



Originally published as:

Lopez Comino, J. A., Cesca, S., Heimann, S., Grigoli, F., Milkereit, C., Dahm, T., Zang, A. (2017):  
Characterization of Hydraulic Fractures Growth During the Äspö Hard Rock Laboratory Experiment  
(Sweden). - *Rock Mechanics and Rock Engineering*, 50, 11, pp. 2985—3001.

DOI: <http://doi.org/10.1007/s00603-017-1285-0>

## **Characterization of hydraulic fractures growth during the Äspö Hard Rock Laboratory experiment (Sweden)**

**J. A. López-Comino<sup>1</sup>, S. Cesca<sup>1</sup>, S. Heimann<sup>1</sup>, F. Grigoli<sup>2</sup>, C. Milkereit<sup>1</sup>, T. Dahm<sup>1</sup> and A. Zang<sup>1</sup>**

<sup>1</sup> GFZ German Research Centre for Geosciences, Telegrafenberg, D-14473 Potsdam, Germany.

<sup>2</sup> ETH Zurich, Swiss Seismological Service, Switzerland

Corresponding author: José Ángel López Comino ([jalopez@gfz-potsdam.de](mailto:jalopez@gfz-potsdam.de))

**Published in *Rock Mechanics and Rock Engineering* 2017**

### **Abstract**

A crucial issue to characterize hydraulic fractures is the robust, accurate and automated detection and location of acoustic emissions (AE) associated with the fracture nucleation and growth process. Waveform stacking and coherence analysis techniques are here adapted using massive datasets with very high sampling (1 MHz) from a hydraulic fracturing experiment that took place 410 m below surface in the Äspö Hard Rock Laboratory (Sweden). We present the results obtained during the conventional, continuous water-injection experiment HF2 (Hydraulic Fracture 2). The resulting catalogue is composed of more than 4000 AEs. Frequency-magnitude distribution from AE magnitudes ( $M_{AE}$ ) reveals a high b-value of 2.4. The magnitude of completeness is also estimated approximately  $M_{AE}$  1.1 and we observe an interval range of  $M_{AE}$  between 0.77 and 2.79. The hydraulic fractures growth is then characterized by mapping the spatiotemporal evolution of AE hypocentres. The AE activity is spatially clustered in a prolate ellipsoid, resembling the main activated fracture volume ( $\sim 105 \text{ m}^3$ ), where the lengths of the principal axes ( $a = 10 \text{ m}$ ;  $b = 5 \text{ m}$ ;  $c = 4 \text{ m}$ ) define its size and its orientation can be estimated for a rupture plane (strike  $\sim 123^\circ$ , dip  $\sim 60^\circ$ ). An asymmetric rupture process regarding to the fracturing borehole is clearly exhibited. AE events migrate upwards covering the depth interval between 404 and 414 m. After completing each injection and reinjection phase, the AE activity decreases and appears located in the same area of the initial fracture phase, suggesting a crack-closing effect.



Originally published as:

Lopez Comino, J. A., Cesca, S., Heimann, S., Grigoli, F., Milkereit, C., Dahm, T., Zang, A. (2017):  
Characterization of Hydraulic Fractures Growth During the Äspö Hard Rock Laboratory Experiment  
(Sweden). - *Rock Mechanics and Rock Engineering*, 50, 11, pp. 2985—3001.

DOI: <http://doi.org/10.1007/s00603-017-1285-0>

## 1. Introduction

Over the last few decades, it has become clear that numerous human activities could generate seismic activity implying environmental risks, such as induced seismicity (Ellsworth, 2013; Rubinstein and Mahani, 2015). Fluids injection is a common practice to improve the exploitation performance in hydrocarbon fields or geothermal reservoirs increasing the permeability and the surface area of rock which is connected to the wellbore (Economides et al., 2000; Davies et al., 2013). This process, referred as hydraulic fracturing, consists in the high-pressure fluid injection into a target rock formation. When the stress on the hole wall in the direction of the maximum in-situ stress exceeds the tensile strength of rock with increase of the fluid pressure, the fracturing process starts, generating new fractures (hydrofractures). An essential issue is to understand the initiation and growth of induced fractures by fluid injection estimating the size, orientation, potential geometries of rupture, which may be inferred from the migration of microseismicity. However, modeling of fracture properties from hydraulic tests is a complex process and the rupture details at a small case may be difficult to recognize and interpret due to heterogeneity of in situ stresses and existence of preexisting cracks. Numerical geomechanical modeling provides a means of including key aspects of natural complexity in simulations of hydraulic fracturing (Smart et al., 2014). On the other hand, traditional approaches map the fracture extension using the hypocentres of induced seismicity (House 1987; Baisch and Harjes 2003; Fischer et al., 2008). The hydraulic fracture growth has been mapped at different scales such as hydrocarbon and geothermal exploitation covering rock volumes of several hundreds of meters (e.g. Suckale 2009; Zang et al. 2014) and mine scale over a few tens of meters (e.g. Maghsoudi et al., 2014).

Our knowledge of hydraulic fractures growth has progressed substantially owing to more intensive high-quality instrumentation. In situ acoustic emission (AE) systems are capable to monitor fractures from meters to centimeters scale during hydraulic fracturing (HF) operations (Kwiatek et al., 2011; Zang et al., 2017). Very weak seismic events, the so-called AE events, are recorded and can reach magnitudes below -7 (McLaskey et al., 2014; Goodfellow and Young, 2014). AE monitoring allows to analyze the growth and properties of hydraulic fractures (Niitsuma et al., 1993; Dahm, 2001; Manthei et al., 2003). Relevant aspects such as asymmetric ruptures can also be identified (Kochnev et al. 2007; Fischer et al. 2008; 2009, Dahm et al., 2010). In addition, in situ rock fracture experiments conducted at underground research laboratories provide the ideal conditions to improve the characterization of hydraulic fractures growth (Goodfellow and Young, 2014; Zang et al., 2017).

We focus this study in the implementation of innovative techniques to detect and locate massive microseismic or AE activity with robust and sufficiently accurate automatic algorithms. These techniques are here applied using a full waveform approach for a hydraulic fracturing experiment (Nova project 54-14-1) that took place 410 m below surface at the Äspö Hard Rock Laboratory, Sweden (Figure 1a). The basic idea of the experiment was to compare hydraulic fracturing growth and induced AE activity under controlled conditions for different fluid-injection schemes: continuous versus progressive fluid injection and dynamic pulse hydraulic fracturing (Zang et al., 2017). Figure 1 shows the location of the experimental tunnel TASN, from where four boreholes were drilled, sub-parallel to orientation of minimum horizontal compressive stress. The middle borehole (blue line in Figure 1) serves as hydraulic testing borehole and was drilled to a total length of 28.40 meter, down dipping  $-4^\circ$ . The remaining

monitoring boreholes were drilled with inclination upwards to allow water outflow from AE sensor chains. This geometry in the predetermined stress state allows hydraulic fractures to propagate perpendicular to the hydraulic testing borehole, in the direction of maximum horizontal compressive stress, and in a direction towards the monitoring boreholes (Zang et al., 2017). The in-situ AE monitoring consists of 11 AE sensors and 4 accelerometers (Figure 1b). AE sensors employed are uniaxial side-view sensors for borehole installation and allow very sensitive recording above 1 Hz (Philipp et al., 2015). The measuring system GMuG AE-System is capable to operate in trigger and continuous mode. For this experiment, the acquisition system for the piezo-electrical sensors has been improved to record continuous signals with 1 MHz sampling rate.

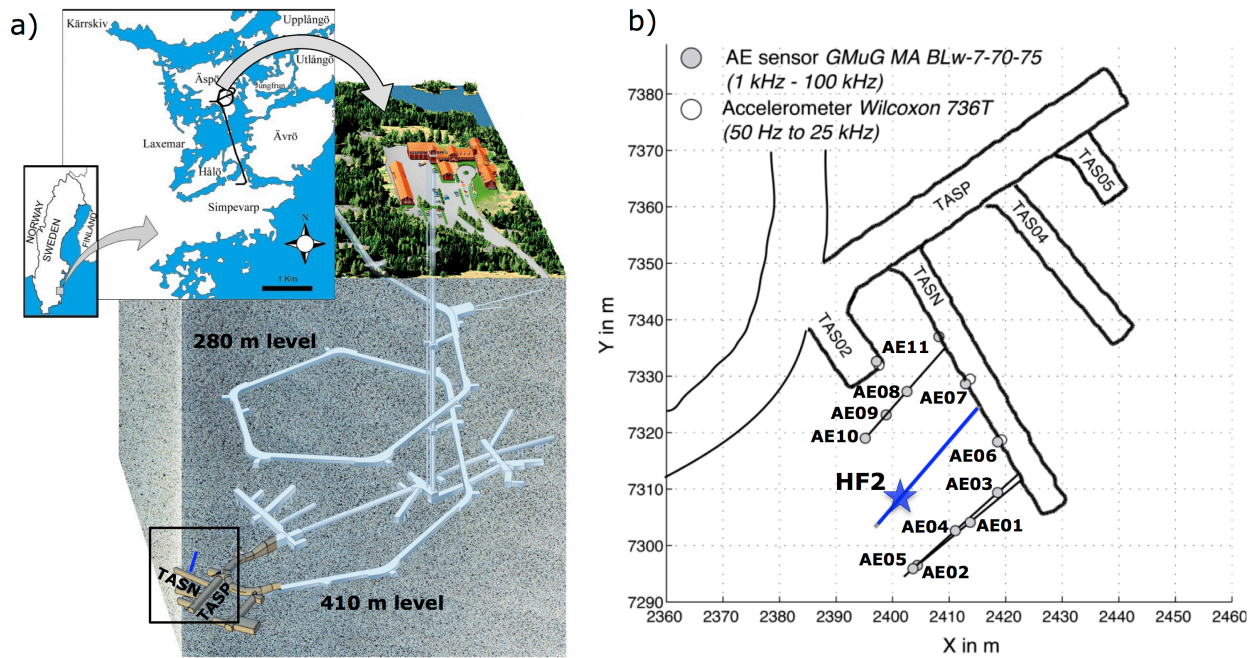


**Figure 1.** a) Test site for hydraulic fracturing in an experimental tunnel of Äspö Hard Rock Laboratory, Sweden [elaborated after [http://www.skb.se/upload/publications/pdf/Aspo\\_Laboratory.pdf](http://www.skb.se/upload/publications/pdf/Aspo_Laboratory.pdf)]. b) Sensors are employed in the near-field: a blue line indicates the hydraulic testing borehole, the blue star identifies the fluid injection segment corresponding to the HF2 experiment.

Zang et al. (2017) described the experiment and provided a reference catalogue of AE hypocenters obtained from four hydraulic fractures based on the in situ trigger and localizing network. We present the results obtained during the conventional, continuous water-injection experiment Hydraulic Fracture 2 (HF2) using the continuous recording mode. HF2 is located at 22.5 m borehole length and recorded the most significant seismicity with 102 AE events relocated in the reference catalogue. In this work, we apply recently developed full waveform stacking and coherence analysis algorithms in order to: i) increase the number of detections; ii) provide robust and accurate automatic relocations; iii) map and characterize the fracture growth identifying the main rupture plane geometries and AE activity migrations.

## 2. Full waveform detection

Hydraulic fracturing monitoring generates massive dataset recording that should be quickly analyzed to detect the induced AE activity. Traditional approaches such as STA/LTA trigger algorithms offer the advantage of rapid analysis using recording in trigger mode for (near) real time assessment. However, weak events could be lost when transient noises are generated in the fracturing area and poor trigger threshold are set with sequences characterized by short inter-event times. Waveform stacking and coherence techniques have been tested for local seismic monitoring and induced seismicity improving the classical detection methods (Matos et al., 2016; López-Comino et al., 2017a). We consider continuous recordings and apply a recently developed automated full waveform detection and location algorithms (Lassie, <https://gitext.gfz-potsdam.de/heimann/lassie>, Heimann et al, 2017).

Lassie is a python-based earthquake detector, which relies on the stacking of characteristic functions (Figure 2). It follows a delay-and-stack approach, where the likelihood of the hypocenter location in a pre-selected seismogenic volume is mapped by assessing the coherence of the P onset times at different stations (Cesca and Grigoli, 2015). Characteristic functions are obtained according to the energy variations calculated from the square amplitudes of each trace (Figure 2b). The stacking of them yields a global characteristic function used to quantify the detector level (Figure 2d) and the coherence values for the preliminary locations (Figure 2c). Lassie has been extended for this specific dataset to analyze very high sampled data (1 Mhz) [see López-Comino et al., 2017b for preliminary results]. The adoption of smooth characteristic function calculated from normalized amplitude envelopes allows to reduce the spatial and temporal sampling. This improves the computational performance of the algorithm and allows its application to high-sampling data as a detector. Even in this condition with 1 Mhz sampling, Lassie was able to process 1 hour of data in 12 hours, on a single workstation (8 processors with 4 cores each one), yielding about 80.000 samples/second. The outstanding computational performance and smooth imaging of the coherence function are achieved at the cost of a larger location uncertainties which accuracy can still be improved upon each event detection by applying different characteristic functions (Grigoli et al., 2013; 2014; see section 3). Preliminary locations are found for each detected event according the maximum value of coherence and the travel-time stacking corrected with P and S-wave velocities (Figure 2c). We have considered a homogeneous full space model where the velocities for both P- and S-waves were obtained from active ultrasonic transmission tests:  $v_p = 5810 \pm 120$  m/s and  $v_s = 3400 \pm 200$  m/s (Zang et al., 2017).

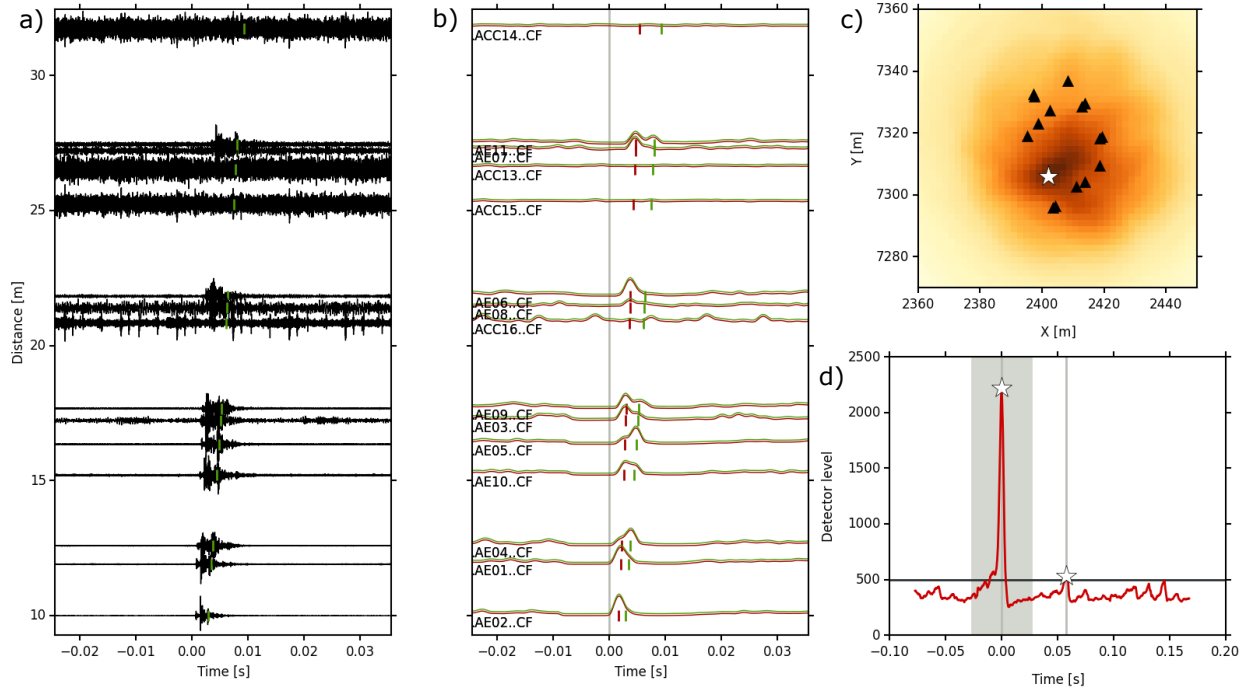


**Figure 2:** Example of acoustic emission detection during the HF2 experiment (the origin time is 08:35:24.477). a) Waveforms sorted by hypocentral distance. b) Characteristic function (normalized amplitude envelopes) for each trace. These are used for travel-time stacking corrected with P-wave speed (red lines) and S-wave speed (green lines). The markers indicate the (best-fit) synthetic arrival time of the respective phases at each sensor. c) Coherence (stack) map for the search region. Dark colors denote high coherence values. The location of the detected event is marked by a white star. Sensor locations are shown with black triangles. d) Global detector level function in a processing time window from -0.1 to +0.2 seconds around the origin time of the detected event. The cut-out time window used for the coherence map is shown in gray color. White stars indicate this and other detection within the same processing time window, exceeding a detector level threshold of 500.

A low detector threshold is chosen, in order not to lose weaker events and enhance the catalogue completeness. However, the small threshold also increases the number of false detections requiring an accurate classification. The dataset has been revised manually, and detected events visually classified in terms of real AE events, electronic noise, anthropogenic noise, long period noise and other signals (Figure 3 and 4). The waveform signatures of most noise events differ clearly from seismic events (figure 3a and 3e). Electronic noise (figure 3b) is found temporally associated with the fluid injection stages. Its occurrence hinders the search of real events. These signals share the same arrivals at all traces and similar frequency content and duration. Classification algorithms matching waveform or spectral patterns may be used for future analysis, but are not considered here. However, noise events generated by workers in the vicinity of the network (figure 3c) are difficult to identify because they display a transient character like seismic events, especially when they were generated by (hammer) blows to the

rock wall or dropping tools. A careful visual inspection is required to consider these aspects. Long period noise (figure 3f) corresponds with harmonic signals are presumably originated inside the monitoring borehole and due to the irregular water inflow. We found other signals that can not fit in the previous families and do not share similar characteristics to establish other possible families. Most of them are detected after the well is shut-in and could also be caused by human factors. However, some of them are observed during phases of constant injection rate: in those cases, they may result by the overlap of electronic noise and weak real events (figure 3e), which hinders their safe classification. Excluding the AE signals and electronic noise, for the remaining types of signals the amplitude of the characteristic function are usually low, so that these events can be easily removed by increasing the detection threshold (e.g. to a value about 750, as shown in Figure 4).

The detection rate results highly discontinuous, with the highest AE detection rates well corresponding to all fluid injection stages (Figure 4). Three AE events are detected during the packer inflation before the initiation of the HF2 experiment. A rapid AE activity increase is experimented when the constant injection rate is applied. Afterwards, a rapid decrease is observed corresponding with few and isolated events. The number of AE events is accounted for the different stages of HF2 (see Table 1 in Section 4), being the Refrac 1 and 5 where the AE activity is largest. Note that the continuous AE recording was not in operation during the whole Refrac 2 experiment and finished prematurely. This explains the detection of only 4 events during this stage.

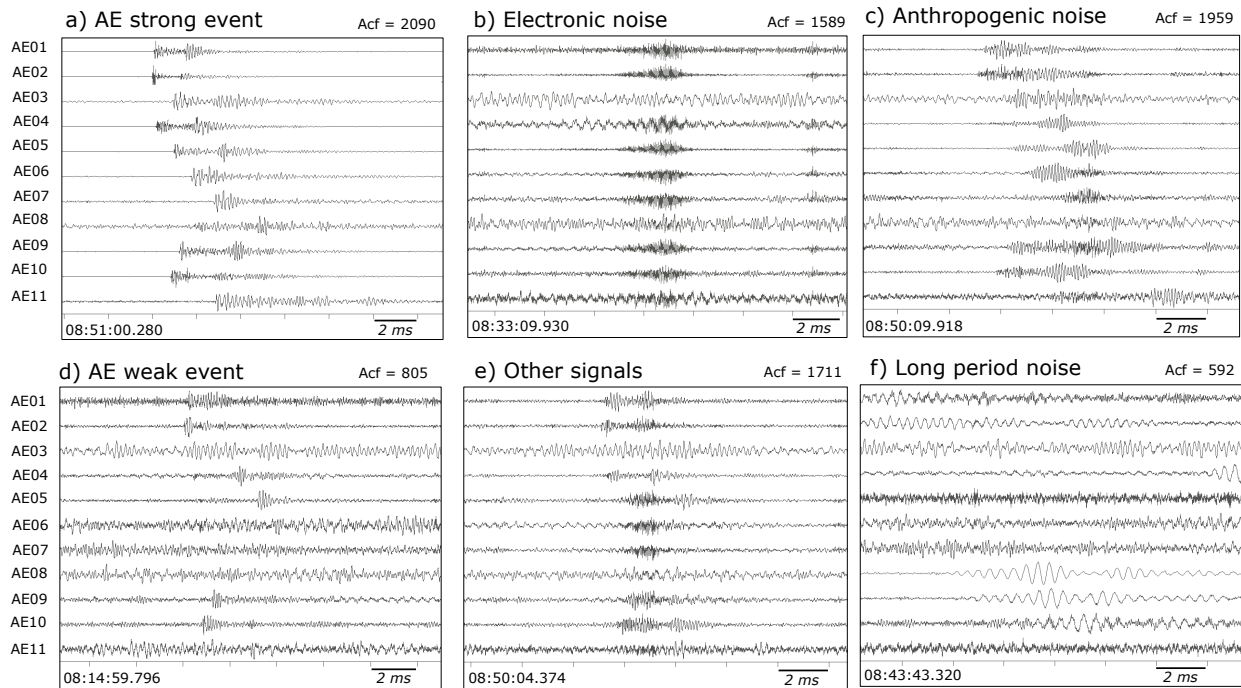


**Figure 3:** Different kinds of detected events by the Lassie algorithm (Heimann et al. 2017) during HF2 experiment. Recorded signals for each acoustic emission (AE) sensor are shown. Amplitude of the characteristic function (Acf) is indicated in the upper right corner of each box. Waveforms are band-pass filtered in the frequency range 3 – 70 kHz. The time (ms) is shown on the x-axis and the reference time is displayed in the lower left corner of each box.

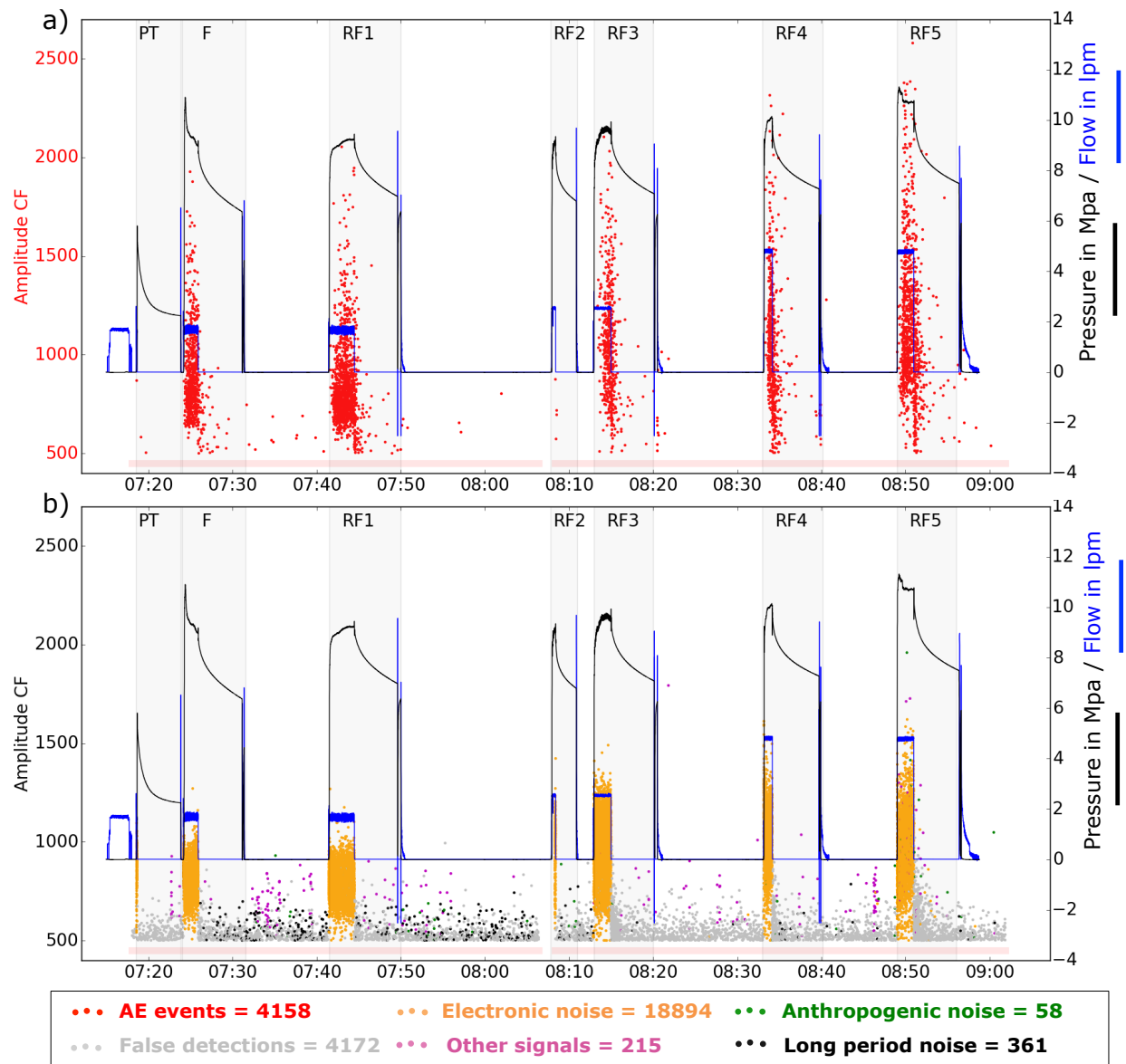


**Figure 4:** a) Acoustic emission events using continuous recordings in the HF2 experiment. b) Other kinds of detected signals from a visual inspection that do not correspond with seismic events. Dots identify different detections according the colors in the legend on the bottom. Amplitude of the characteristic function (left ordinate), injection pressure and flow rate (right ordinate) are shown. Different stages for HF2 are indicated using gray background (PT: Pulse test; F: Frac; RF1 - RF5: Refrac 1 - Refrac 5). Light red line on the bottom for each figure indicates the continuous recording data.

### 3. Automated locations using coherence

Standard automated locations routines are widely used for most seismological applications. Generally, they are based on the automated picking and identification of the seismic phase P and S, searching the iterative minimization of the residuals between the theoretical and observed arrival times of these main seismic phases (Geiger, 1910). However, hydraulic fracturing processes generate bursts of events, which recording are characterized by low signal-to-noise ratio and the locations could lose reliability for the weaker events. Other methodologies such as waveform coherence analysis have been used for mining induced seismicity obtaining successful results (Grigoli et al., 2013). Robust and sufficiently accurate locations are reached with these techniques and can be extended to our dataset allowing credible interpretations about growth and migrations for the hydraulic fractures.

The location of the AE events is further refined using a more accurate waveform stacking method which uses both P and S phases (Grigoli et al., 2014). The proposed method is fully automatic and only requires a few control parameters (maximum and minimum length of the short window, and short to long time window ratio), which can be chosen following a trial and error approach on a small subset of the largest events. A 3D grid is generated around the hydraulic fracturing volume (15 x 15 x 15 m) using a size grid of 10 cm. A multidimensional matrix is retrieved, whose absolute maximum corresponds to the spatial coordinates of the seismic event. The same homogeneous full space model considered for the detections is used. Moreover, the relative location accuracy can be improved using a master event approach (Grigoli et al. 2016). The preliminary absolute location of the largest events shows a clear cluster that delineates the fracture geometry and its spatial extent (Figure 5a). Next, we considered a master event inside this cluster with a very accurate location and high maximal coherence to obtain more accurate the relative locations. This approach reflects a regrouping of the largest localized events around the previously identified cluster (Figure 5a). All AE events, even the weakest, can be located using this technique resulting in a catalogue composed of more than 4000 AEs (Figure 5b). The relative hypocenters are spatially clustered in a planar region, resembling the main fracture plane, which orientation and size can be estimated from the spatial distribution of the AEs (section 5). These results are consistent with those obtained by Zang et al. (2017), from 102 locations only, where the main fracture was identified on the SE side of the HF2 experiment. However, the large number of detections allows us to extend and track the planar rupture down to 414 m depth, instead of 410 m.

We estimated uncertainties according to Grigoli et al. (2013) by assessing the spatial distributions of locations for each event after iteratively repeating the location procedure using a broad range of STA/LTA configuration. The in situ trigger mode estimated the maximum hypocenter location residual in 0.3 m (Zang et al., 2017) and it could be comparable with the hypocentral location errors for the events shown in Figure 5a. In this case, the median uncertainty was lowered from 1.43 to 0.64 m using the master event approach and yielding uncertainties below 0.3 cm according the 25th percentile. As discussed in Grigoli et al. (2016) the accuracy of the relative location may be spatially dependent, increasing with the distance to the location of the master event. On the other hand, while traditional methods for visualization and interpretation of seismicity only consider the punctual information contained in each data point (i.e the spatio-temporal coordinates of each seismic event), the Kernel Density Estimator

(KDE) allows to visualize massive seismicity data with the advantage that location uncertainties and mislocated events are fully taken into account. The KDE approach extends the method discussed in Cesca et al. (2016) for an aftershock sequence, which was based on the stack of coherence maps. In this context the KDE results a more objective visualization tool, in comparison to standard plots, which show the seismicity distribution only.

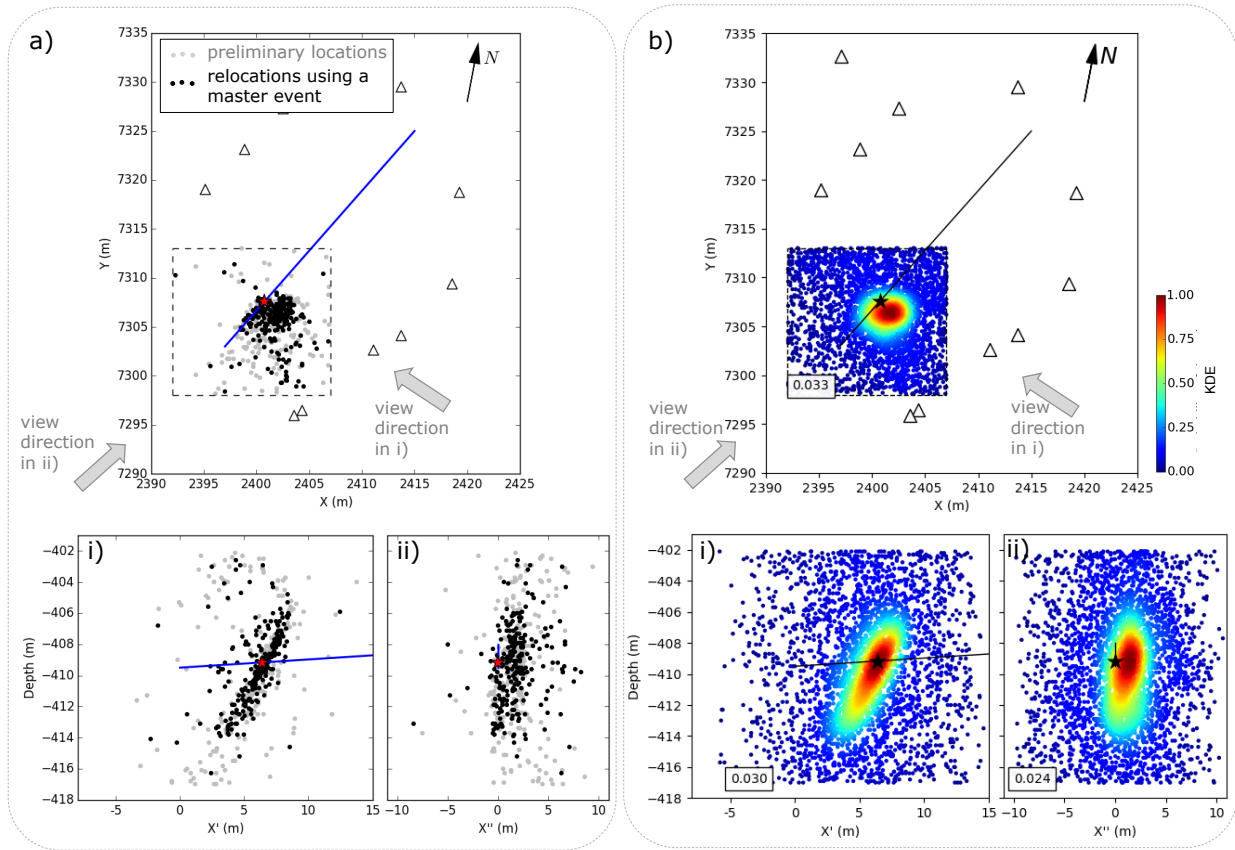


**Figure 5.** a) Small subset of the largest AE events (amplitude of characteristic function larger than 1500, in total 258 AEs, see Figure 4) is located with two techniques: waveform coherence analysis (gray dots) and relocation using a master event (black dots). Blue line and red star show the fracturing borehole and the location of the HF2 experiment, respectively. b) All AE events relocated using a master event (4158 AEs), showing the Gaussian Kernel density where red denotes higher density and blue regions with few events. This Kernel Density Estimator (KDE) shows the probability density function according the spatial distribution of the hypocenters for each plot. A normalized color bar scale is used for all plots; the absolute maximum value of the KDE is indicated on the lower right corner for each plot. Black line and black star show the fracturing borehole and the location of the HF2 experiment, respectively. a) and b) show the map view on the top and two side views on the bottom: i) perpendicular to the fracturing borehole and ii) along the fracturing borehole. The square with dashed line in map view indicates the search area used in the location. Note the location searching on depth is limited between -402 and -417 m.

#### 4. Frequency-magnitude distribution

The frequency-magnitude distribution (FMD) is an important feature of the observed seismicity that can be described by a power law such as the Gutenberg-Richter distribution proposed for earthquake catalogues (Gutenberg and Richter, 1944). This scaling relation seems to hold to very small magnitude events such as -4.1 when AE sensors are used (Kwiatek et al., 2011). We investigate the FMD estimating the AE magnitude for our complete catalogue. Eisenblätter and Spies (2000) propose a relative magnitude in dB, which is not comparable with common seismological scales. This approach was used for the 102 relocated AE events detected from the trigger mode in the HF2 experiment, yielding an AE magnitude range between 24 to 49 dB (Zang et al., 2017). To evaluate the FMD for the AE events in terms of the logarithm of maximum amplitudes, AE amplitudes reported in dB were divided by 20 and, thereby, we can produce the same form of the Gutenberg-Richter relation (Cox and Meredith, 1993). The size of the events is determined using the maximum amplitudes of the 11 AE sensor signals and the distances from the AE sources to the sensors, where the mean amplitude is defined as the amplitude value of the linear regression curve at a reference distance of 20 m from the source (Köhler et al., 2009). Note that we used the same scaling parameter and damping as in Zang et al., 2017 to calculate the mean amplitude, but use the maximal amplitude of the full waveform instead than from the P phase only. Similarly, we obtain absolute and dimensionless AE magnitudes ( $M_{AE}$ ) that can be directly used to evaluate the FMD.

This common approach allows to estimate b-values and magnitude of completeness ( $M_c$ ) of AE events from the FMD (Cox and Meredith, 1993; Becker et al., 2010; Maghsoudi et al., 2013; 2014). Figure 6 shows the  $M_{AE}$  estimations for our complete catalogue, with values ranging between  $M_{AE}$  0.77 and 2.79. Assuming empirical energy relations (Eisenblätter and Spies, 2000),  $M_{AE}$  range between 0 and 5, would roughly correspond to moment magnitudes between  $M_w$  -8 and -3. Therefore, our relative magnitude range corresponds with pico-, femto- and atto-seismicity and reveal fracture dimensions of millimeter to decimeter scale [Bohnhoff et al., 2009, table 1 therein]. Note that we will refer as AE activity in this work. A progressive increment of the  $M_{AE}$  was observed during the whole HF2 experiment (Zang et al. 2017). We confirm this observation: the largest event corresponds with  $M_{AE}$  of 1.94 during the initial fracture phase (“Frac” stage) and 2.79 during the propagation of the fracture in the final stage (“Refrac 5”) (Table 1). On the other hand, b-values and  $M_c$  are estimated according Wiemer and Wyss, 2000 (Figure 7). We obtain a high b-value of 2.38 and a  $M_c$  of 1.1. In addition, these values are calculated for the different experiment stages in order to identify other possible relationships (Table 1 and Figure 8). The largest b-value (3.52) is obtained initially in the “Frac” stage and the smallest (1.85) for the “Refrac 4” stage.  $M_c$  does not show large variations for the different stages, resulting in values between 1.0 and 1.25. Apparently, we do not find relationships between the number of the events and the b-value. Another interesting issue is to check relation between the injected volume and the seismicity parameters (Figure 8, see section 6).

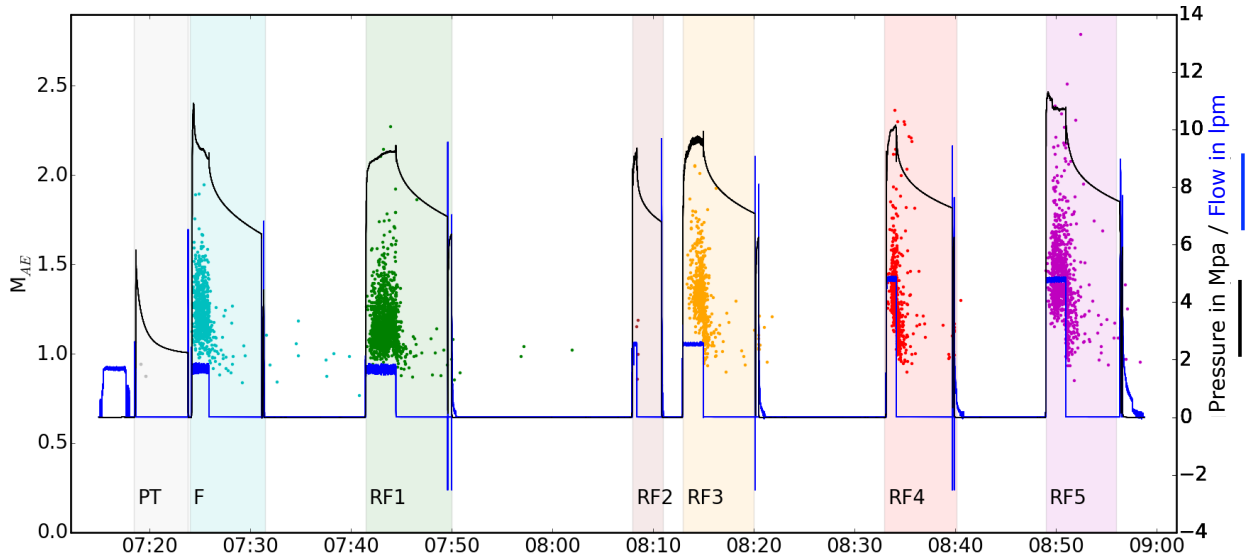


**Figure 6.** Distribution of the AE events according to the AE magnitude for the whole HF2 experiment. AE events are identified for different colors according to the different stages for HF2: PT (Pulse test, gray), F (Frac, blue), RF1 (Refrac 1, green), RF2 (Refrac 2, brown), RF3 (Refrac 3, orange), RF4 (Refrac 4, red) and RF5 (Refrac 5, purple). Different stages for HF2 are also indicated using the background colors previously defined.

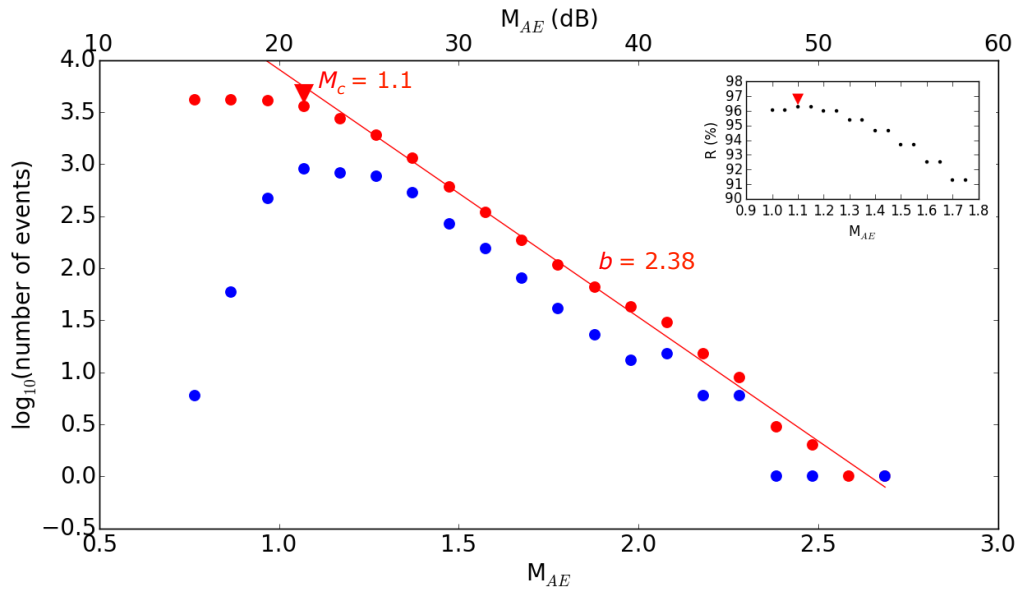


**Figure 7.** Frequency-magnitude distribution (FMD) of the overall catalogue for the HF2 experiment. Red line shows the best fit for the cumulative FMD (red dots), indicating the b-value and the magnitude of completeness ( $M_c$ ). Non-cumulative FMD is also shown with blue dots. On the upper right corner, we show the goodness of the fit with the absolute difference,  $R$ , of the number of events in each magnitude bin between the observed and synthetic distribution (see equation 2 in Wiemer and Wyss, 2000). The  $M_c$  selected (inverted red triangle) is the magnitude at which  $R$  is maximum.

Experiment	N° events	$M_{AE,max}$	$M_{AE,min}$	$M_c^*$	$M_{c,max}(t)^{**}$	N ( $M_{AE}>1.25$ )	N ( $M_{AE}>1.6$ )	b-value*	$V_i$ (l)
HF2	4158	2.79	0.77	1.10	1.61	2068	288	2.38	29.7
Pulse text	3	1.06	0.87	-	-	0	0	-	-
Frac	690	1.94	0.77	1.15	1.37	291	12	3.52	3.8
Refrac 1	1325	2.27	0.85	1.05	1.32	288	22	2.60	5.0
Refrac 2	4	1.18	1.14	-	-	0	0	-	1.2
Refrac 3	551	2.05	0.9	1.25	1.40	354	44	3.12	5.5
Refrac 4	595	2.36	0.9	1.00	1.54	348	45	1.85	4.8
Refrac 5	990	2.79	0.85	1.25	1.61	787	165	2.17	9.4

\*Calculated from Wiemer and Wyss, (2000)

\*\*Calculated from Hainzl, (2016)

**Table 1.** Comparison for the different stages of the HF2 experiment: number of events, maximum ( $M_{AE,max}$ ) and minimum ( $M_{AE,min}$ ) AE magnitude, magnitude of completeness ( $M_c$ ) using different techniques (we indicate the maximum value for the rate-dependent completeness magnitude  $M_c(t)$  from Hainzl, 2016, see figure 9), number of events above of  $M_c$  1.25 and 1.6 (maximum  $M_c$  values from Wiemer and Wyss, 2000 and Hainzl 2016, respectively), b-value and injected volume ( $V_i$ ). Note that the continuous AE recording was not fully operational during the whole experiment Refrac 2.

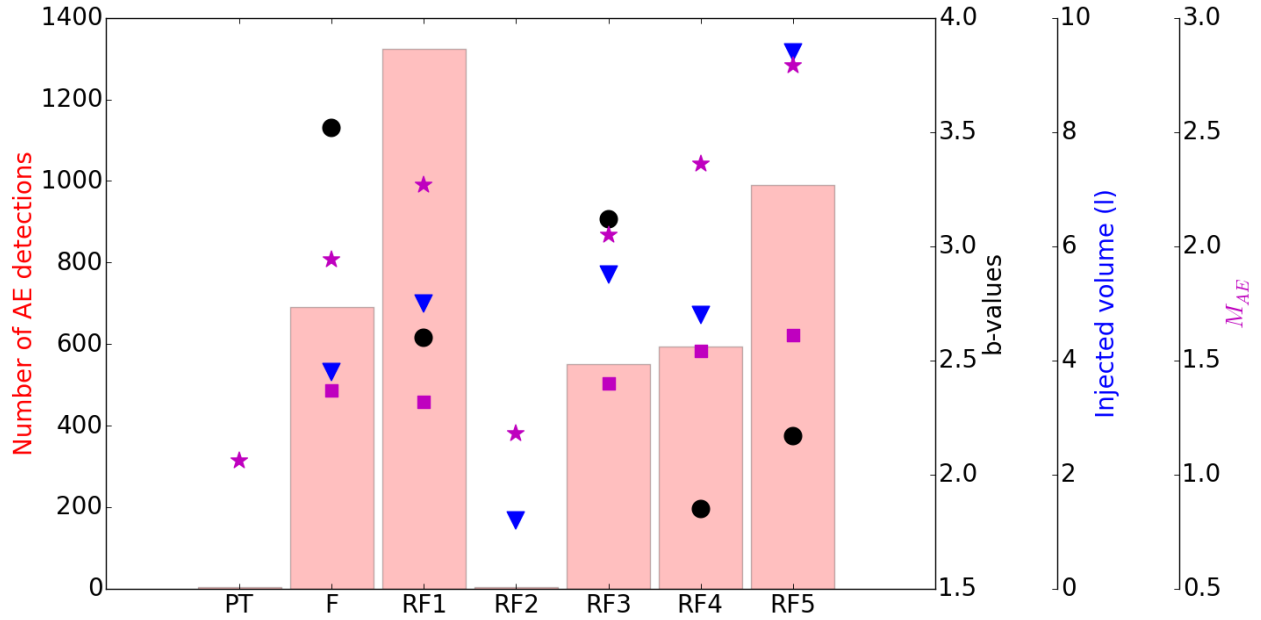


**Figure 8.** Comparison for the different stages during the HF2 experiment: number of events (red bars), maximum  $M_{AE}$  (magenta stars), maximum value for the rate-dependent completeness magnitude  $M_c(t)$  from Hainzl, 2016 (magenta squares), b-value (black dots) and injected volume (blue inverted triangles). Note that the continuous AE recording was not fully operational during experiment Refrac 2, therefore the maximum  $M_{AE}$  and the number of events is not representative.

High AE activity phases are identified for the HF2 stages. Hainzl (2016) showed that such high seismicity rates could reflect an apparent decrease of the estimated Gutenberg-Richter b value and short-term increases of  $M_c$  above a basic completeness magnitude ( $M_{c0}$ ). We apply the method of Hainzl (2016) to account for these effects and estimate the rate dependent completeness magnitude,  $M_c(t)$  (Figure 9).  $M_{c0}$  of 1.1 is assumed from the maximum-curvature technique used previously (Figure 7). The binning interval of reported magnitudes of 0.01 and 10-neighbor events are considered for calculating. Estimated b values for  $M_c(t)$  are calculated for different threshold rates  $r_{max}$  (Figure 9a). Stable b values of  $2.57 \pm 0.05$  are found for rates below 300 events/minute, but b values start to decrease for larger rates similarity to the results for the aftershock sequences and earthquake swarms (Hainzl., 2016). In Figure 9b, the estimated variation of  $M_c(t)$  is shown as a red curve for  $r_{max}=300$  and reflect increases of  $M_c$  during the fluid injection in each stage reaching a maximum value of  $M_c = 1.61$  (the maximum values for the  $M_c$  are reported in table 1). A slight progressive increment of the  $M_{cmax}(t)$  is observed during the whole HF2 experiment, which is coherent with the increase of the  $M_{AEmax}$  (Table 1 and Figure 8).

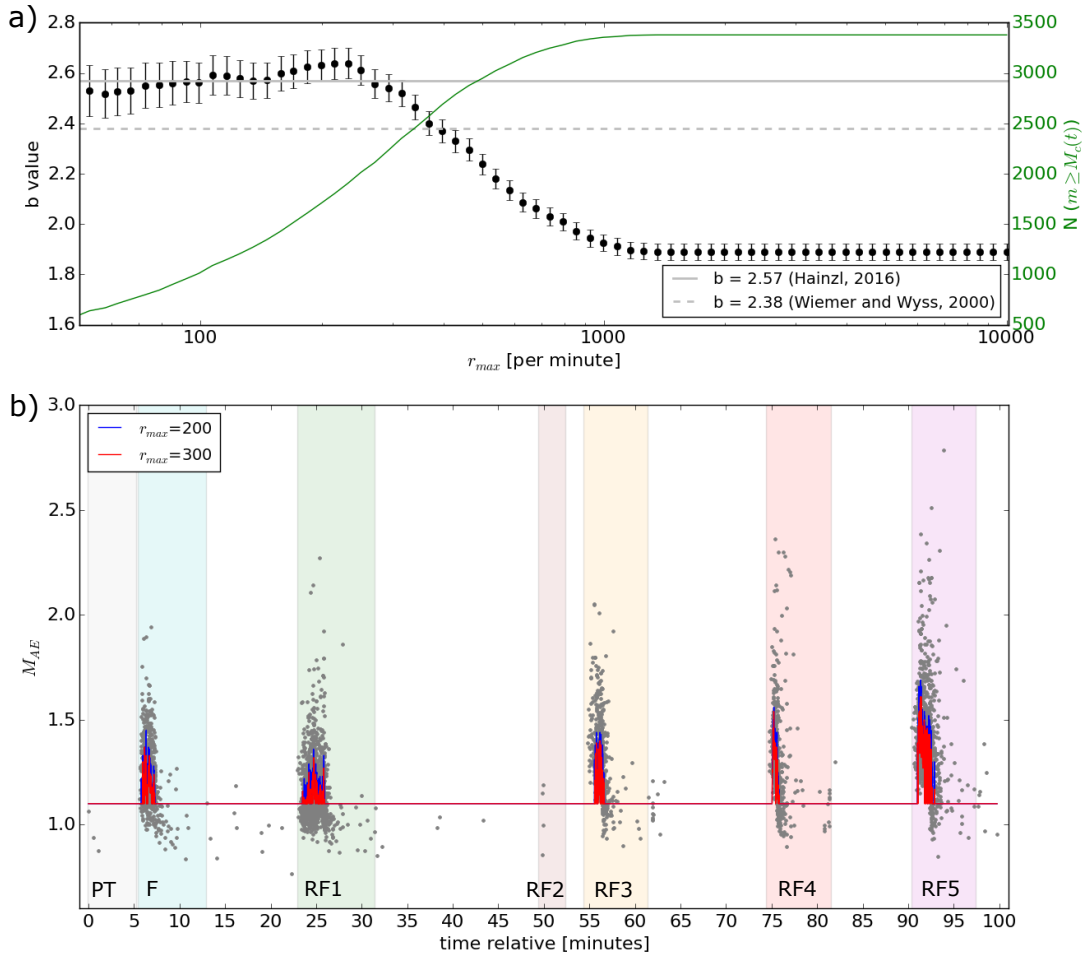


**Figure 9.** Applications of the algorithm from Hainzl, (2016) to estimate the rate-dependent completeness magnitude  $M_c(t)$ . a) Estimated b-values for  $M_c(t)$  calculated for different threshold rates  $r_{max}$ , showing stable results for values smaller than approximately 300 events/minute, in which horizontal line refer to  $b = 2.57$ . Dashed horizontal line shows the b-value = 2.38 using the maximum-curvature technique (see figure 7). Right ordinate indicates the number of events ( $N$ ) with magnitude larger than  $M_c(t)$ . b) Estimations of  $M_c(t)$  for  $r_{max} = 200, 300$  events/minute applied to all events in the HF2 experiment (blue and red lines, respectively). Gray dots indicate recorded AE events with their magnitudes. Different stages for HF2 are also indicated using the background colors defined in figure 6.

## 5. The fracture growth process

The parameters of the hydraulic fracture, such as the rupture length and width, the rupture plane orientation and their temporal evolution can be estimated by mapping the fracture extension using the induced microseismicity (e.g. Kochnev et al. 2007; Fischer et al. 2008). Preliminary results from the in situ trigger mode showed AE events migrating upwards outline a plane (strike  $133^\circ$ , dip  $62^\circ$ ) extending up to 6.7 m away from the fracturing borehole (Zang et al., 2017). Based on the previous analysis of AE events from continuous recording, we have a more complete catalogue with robust locations to improve the previous results. The spatial distribution of the AE events is clustered resembling an ellipsoid (Figure 5). A best fitting rupture plane can be identified considering the locations of the largest AE events (e.g.  $M_{AE} > 1.5$ ) inside the cluster volume (Figure 10). A minimum search algorithm (`scipy.optimize.curve_fit`, which use a non-linear least squares to fit a function, see <http://www.scipy.org/>) is applied to get the plane equation. The fracture plane has a strike of  $123.6^\circ$  and a dip of  $55.6^\circ$ , an orientation compatible to the one stated by Zang et al., 2017, where the fracture orientation from the impression packer indicated a strike of  $123^\circ$  and dip of  $60^\circ$ . Figure 11 displays the location of the AE events following the characteristic of the main rupture plane, showing the side views along the plane azimuth and perpendicular to the plane. The ellipsoidal shaped cluster of hypocenters can be used to characterize the spatial extension of the main fracture assuming the area where the Gaussian Kernel density is larger than 50% (green, yellow and red zones in figure 11). This is quantified according the principal axes of length:  $a = 10$  m;  $b = 5$  m;  $c = 4$  m (see labels in first column of the Figure 11) Note that the main rupture volume corresponds with this ellipsoid ( $\sim 105$  m<sup>3</sup>), but the rupture extension could be even larger considering all locations of the AE events, some of which appear to be more spatially scattered. This prolate ellipsoid ( $b \approx c$ ) shows an asymmetric rupture whose center is located about 1 m away from starting of the HF2 experiment (see eccentricity,  $e$ , in Figure 11).

Next, the AE activity migration is analyzed to characterize the hydraulic fracture growth considering the different stages of the HF2 experiment (Figure 11). AE events migrate generally upward through different stages. For each stage, they outline smaller ellipsoids whose centers (points with maximum Gaussian Kernel density) are slowly moving upward, from a depth of  $\sim 412$  m at the beginning of the experiment to a depth of  $\sim 408$  m at the end of HF2. The initial fracture phases (Frac and Refrac 1) cover the depth interval between 408 and 414 m; the lower tip of the fracture is extended to 404 m depth during the last stage (Refrac 5). In addition, we can analyze the small temporal scale migration within each stage, to discuss its time dependence with respect to fluid injection and fluid pressure changes. More details can be depicted for the stages with more abundant AE events. Therefore, we show here the results for Refrac 1 and Refrac 5 (Figure 12). Refrac 1 reflects the same pattern identified for the whole experiment, with the seismicity moves upward (Figure 12a). Refrac 5 also shows an upward migration pattern, reaching the shallower seismicity during the constant injection rate. However, the seismicity moves downward at the end of the experiment, covering the depth interval between 411 and 414 m (Figure 12b).

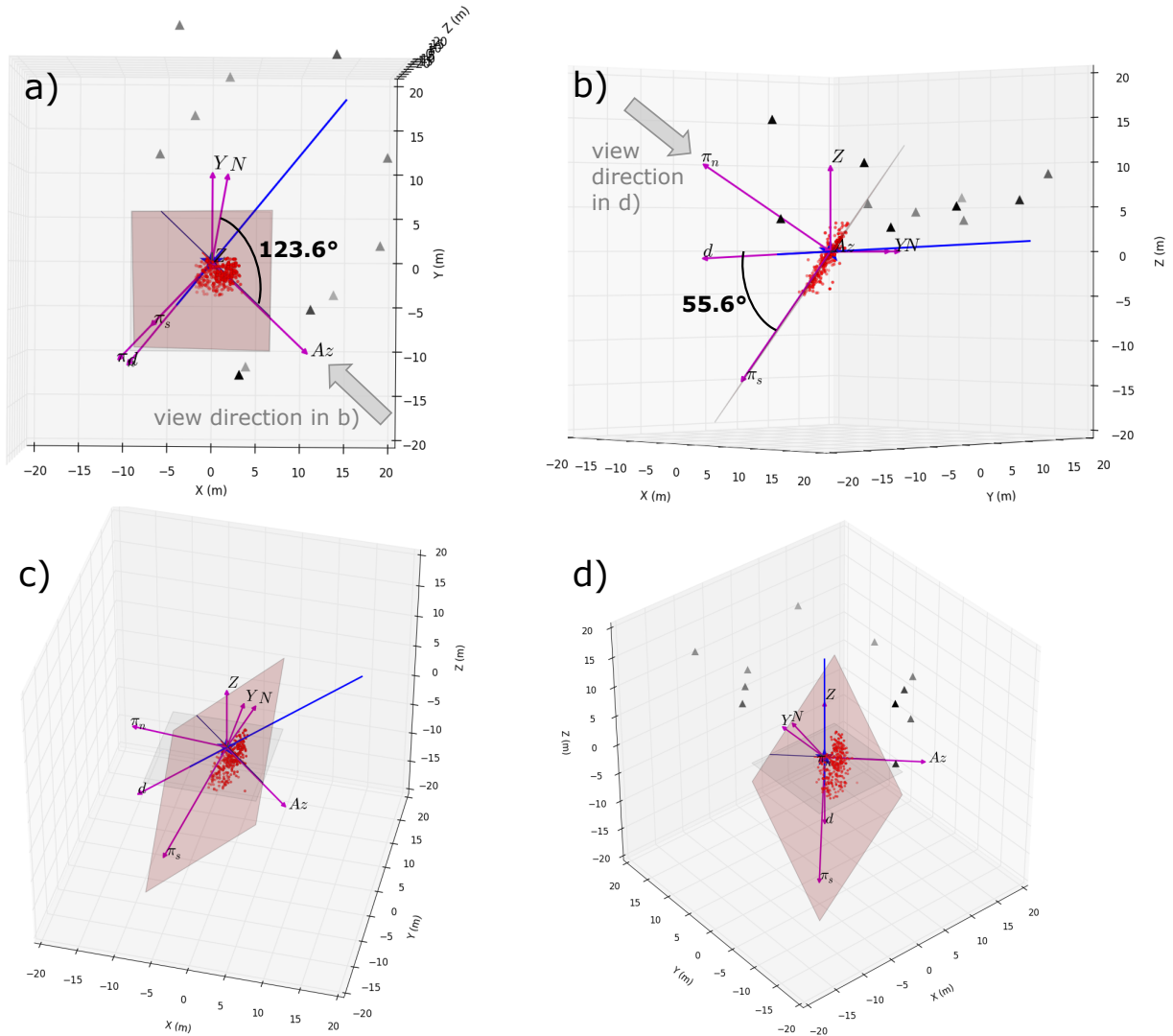


**Figure 10.** 3D views for the main rupture plane (red plane) that is defined considering the locations of the largest AE events ( $M_{AE} > 1.5$ ) inside the cluster volume (red dots) identified from the Figure 5 (in total 318 AE events): a) view from above; b) side view along the azimuth of the rupture plane; c) perspective view and d) side view perpendicular to the rupture plane. The location of the HF2 experiment is represented by a black star and corresponds with the reference point for this Cartesian coordinate system. We show the following vectors in magenta color: Y, Z, N (north), d (fracturing borehole direction), Az (azimuth for the rupture plane),  $\pi_n$  and  $\pi_s$  (perpendicular and the steepest slope for the rupture plane). Horizontal plane in light gray color is also show as reference whose intersection with the rupture plane (black line) indicates the azimuth direction. AE sensors and the fracturing borehole are also shown using black triangles and a blue line.

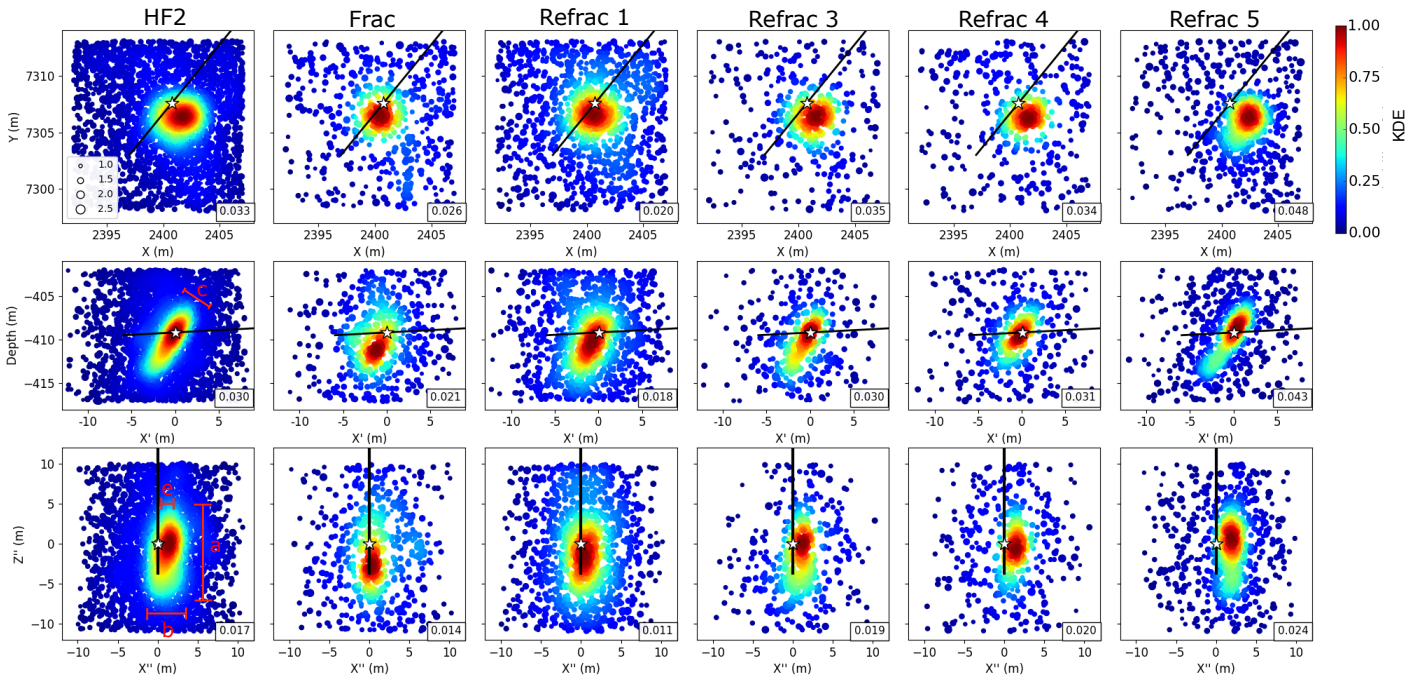


**Figure 11.** The fracture growth is analyzed from the locations of the AE event showing the Gaussian Kernel density where red denotes a higher density of AE sources and blue regions with few events. This Kernel Density Estimator (KDE) shows the probability density function according the spatial distribution of the hypocenters for each plot. A normalized color bar scale is used for all plots; the absolute maximum value of the KDE is indicated on the lower right corner for each plot. Results are shown for different stages: whole HF2 experiment (first column), initial fracture phase (Frac, second column) and the propagation of the rupture during different refracturing (Refrac 1, 3, 4 and 5 - third to sixth columns). Dots are scaled according the  $M_{AE}$  (see legend in the first box). Three perspective views are shown: view from above (first line), side view along the azimuth of the rupture plane (second line, see figure 10b) and side view perpendicular to the rupture plane (third line, see figure 10d). We characterize an ellipsoid where the seismicity is clustered through its principal axes (a, b, c) and whose center is located about 1 m (eccentricity, e) away from starting of the HF2 experiment (see labels in first column). Location of the HF2 experiment and fracturing borehole are shown by a white star and a black line.

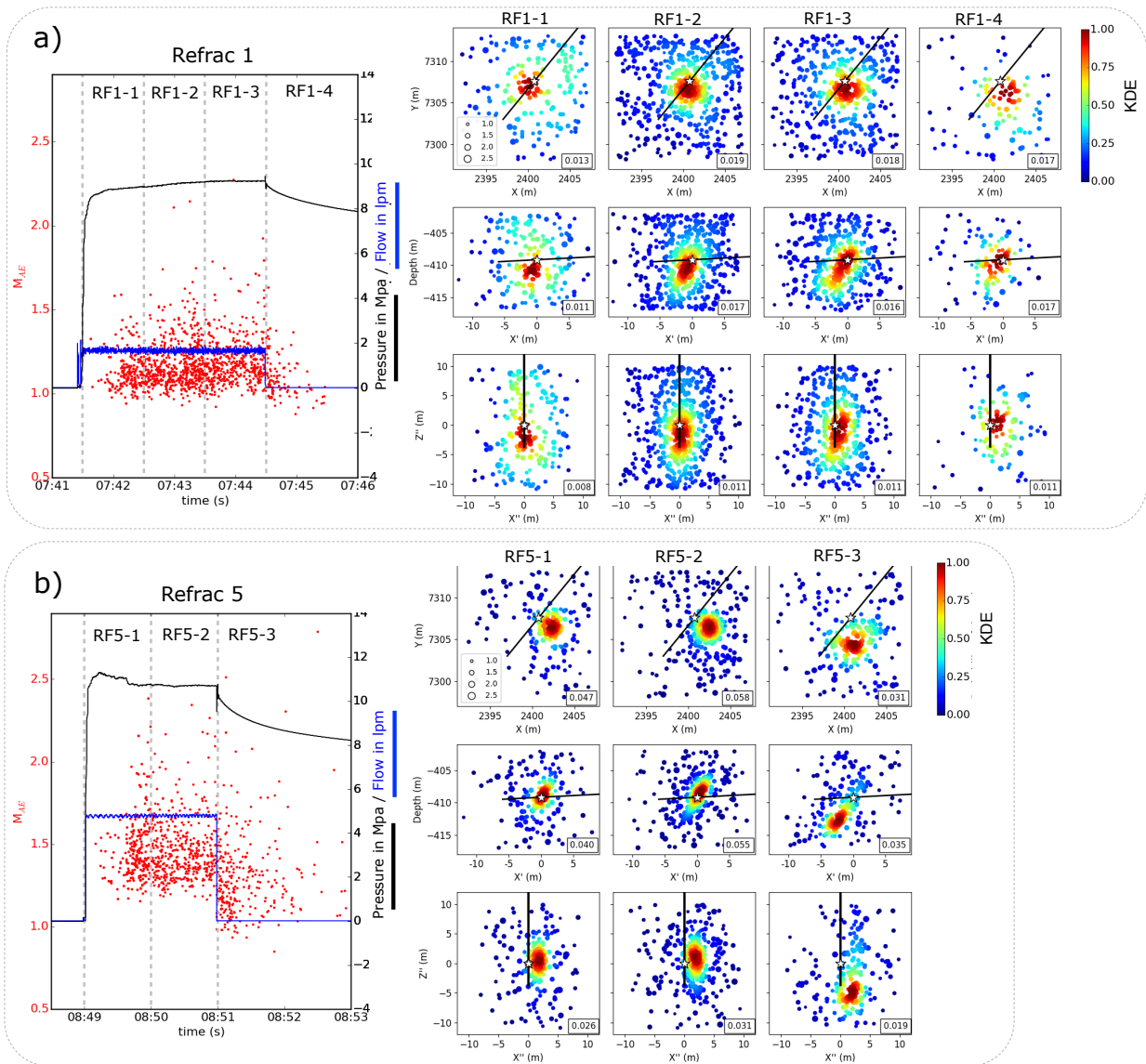


**Figure 12.** The small temporal scale fracture growth is analyzed for the propagation of the rupture during selected phases: (a) Refrac 1 and (b) Refrac 5, where most AEs take place. On the left side, AE detections for each stage according the  $M_{AE}$  (red dots). Detections are divided for each minute according the dashed gray lines. Full time scale as seen in Figure 6. On the right side, locations of the AE events showing the Gaussian Kernel density where red denotes higher density of AEs and blue regions with few events. This Kernel Density Estimator (KDE) shows the probability density function according the spatial distribution of the hypocenters for each plot. A normalized color bar scale is used for all plots; the absolute maximum value of the KDE is indicated on the lower right corner for each plot. Each column considers the AE events for one-minute duration (see division of the figure on the left side). Dots are scaled according the  $M_{AE}$  (see legend in the first box). Three perspective views are shown: view from above (first line), side view along the azimuth of the rupture plane (second line, see Figure 10b) and side

view perpendicular to the rupture plane (third line, see Figure 10d). Location of the HF2 experiment and fracturing borehole are shown by a white star and a black line.

## 6. Discussion

The automated detection and accurate location of AE events are crucial to describe the progress and growth of hydraulic fractures. Traditional approaches using recording in trigger mode for (near) real time assessment are essential for rapid interpretations to decide about the next operations for hydraulic fracturing. However, weak and simultaneous events could be lost or their phases not properly associated. Indeed, the largest possible number of events should be detected and considered for advanced analysis to understand the behavior, extension and growth of hydraulic fractures. Waveform stacking and coherence techniques (Heimann et al., 2017, Grigoli et al. 2016) have been here adapted to detect and locate AE sources for massive datasets with very high sampling (1 MHz). Using continuous waveforms we are able to identify a large number of events, even in presence of AE activity bursts, when multiple events occur close in space and time. Moreover, our approach is based on the detection of coherent increased in waveform amplitude at multiple sensors, being able to detect events even in presence of noise contaminated data. At this respect, it should be noted that a triggered based approach (Zang et al., 2017) was able to detect and locate 102 events in the same dataset, after removal of artificial sources, whereas our catalogue of located frac-induced AE events is more than 40 times larger (4158 events). The detection threshold is the most relevant parameter which influences the detection performance of the used algorithm. A low threshold allows the detection of weak events at the cost of a higher number of false detection and noise signals of different types. In this sense, it is desirable that the detection setup can be in future combined with a classification algorithm to distinguish true and false events, and classify different signals in an automatic manner, e.g. using hidden Markov models that have already been introduced in the field of induced seismicity (Beyreuther et al., 2012). At this stage, we performed a manual classification, dividing the detections in five categories: real AE events, electronic noise, anthropogenic noise, long period noise and other signals. The inspection of the temporal evolution of signal detection reveals that 85% of AEs take place during the phases of increased flow rate and increasing pressure, dropping very quickly in time as soon as the pressure decrease and the flow stopped. In the time periods between each fracture and refracture operations, very few and weak events are detected.

A complete catalogue of AE events is obtained in an underground experiment with hydraulic fracture growth in naturally fractured crystalline rock. Our catalogue allows to estimate the  $M_{AE}$  in order to evaluate the FMD. High b-value ( $\sim 2.4$ ) is obtained for the HF2 experiment, reflecting similar characteristics observed in salt mining induced microseismicity (Maghsoudi et al, 2014). A deficit of larger events linked to the constant injection rate during a limited time could be associated with this high b-value. A slight decrease of the b-values is shown for the different stages of the HF2 experiment (Figure 8). The maximum observed magnitude increases with time in the fracturing experiment reaching its maximum value ( $M_{AE, max} 2.79$ ) at the end of the experiment (Refrac 5) when the injected volume is largest. The overall  $M_c$  is estimated around 1.1, but we observe a minimum value of  $M_{AE, min} 0.77$ . The rate-dependent incompleteness of our catalogue reveals a decrease of the b values for larger AE activity rates, as found for aftershock sequences and earthquake swarms (Figure 9a). The observed slight progressive increment of  $M_{cmax}(t)$  appears related with the increase of the  $M_{AEmax}$  during the whole HF2 experiment (Figure 8). Furthermore, during the refracturing phases with the largest events (Refrac 4 and 5), we observe a temporal decay of  $M_c(t)$ , a pattern observed for aftershock

sequences triggered by a mainshock that are much larger in magnitude than the detection threshold of the seismic network (Hainzl, 2016) (Figure 9b).

Figure 13 and 14a discusses the relation between injected volume and seismicity parameters. The maximum magnitude in each frac / refrac phase appears to be correlated to the injected volume (Figure 13a); this support observations for moderate injection induced seismicity (McGarr, 2014), but never discussed for AE activity. No clear correlation could be found, in change, between the injected volume and other seismicity parameters, such as b-value and number of AEs events (Figure 13b and 13c). McGarr (2014) suggested that the maximum experience magnitude of injection induced seismicity should not overcome a bound which linearly increases with the injected volume. This relation seems to hold for our case (Figure 14a). Assuming the relation proposed by McGarr (2014) and the overall injected volume of 29.7 l during HF2, one would expect that the maximum magnitude should not exceed a value of  $M_w = -0.06$ . Since we cannot easily convert  $M_{AE}$  estimates into equivalent moment magnitudes, we consider that the maximum induced AE event during HF2 would correspond to the worst case scenario of a rupture involving the whole length of the imaged fracture, which is equal to 10 m (the value of the largest principal axe of the ellipsoid identified from the AE locations). Using the source model of Madariaga (1976) and a stress drop  $\Delta\sigma = 3$  MPa (McGarr 2014, also consistent with the stress drop range suggested by Kwiatek et al., 2011, and Goodfellow and Young, 2014), we obtaine a magnitude  $M_w$  of -0.08, compatible with the magnitude limit suggested by McGarr (2014). On the other hand, Dahm et al. (2008) show an empirical relation for the maximal induced earthquakes as a function of the size of the seismicity cloud or, if otherwise estimated, the size of the intrusion (Figure 14b). In that case, the worst case scenario would reveal a more realistic  $M_w$  of -3.07 if we compare it with the observed largest AE event ( $M_{AE, max}$  2.79 corresponding to  $M_w$  around -5, Eisenblätter and Spies, 2000). This finding would support that an upper bound for the maximum expected magnitude down to the magnitude scale of AEs. However, it should be noted that an accurate calibration of the AE sensors and their coupling would be needed to develop a robust relation between  $M_{AE}$  and  $M_w$ .

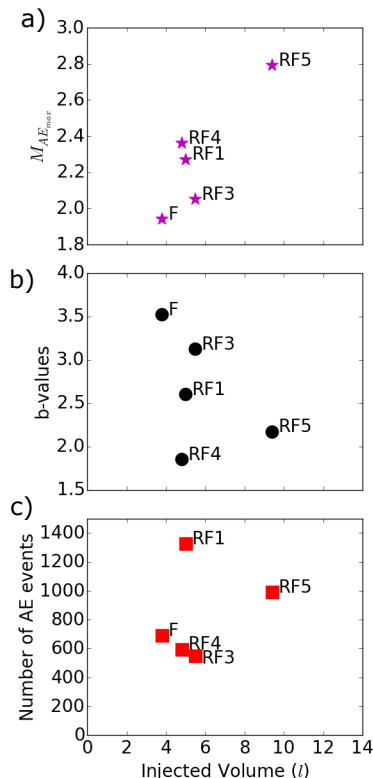


**Figure 13.** Maximum AE magnitude (a), b-values (b) and number of AE events (c) as functions of the volume of injected fluid (in liters) for the initial fracture phase (F) and the propagation of the rupture during different refracturing (RF1, RF3, RF4 and RF5).

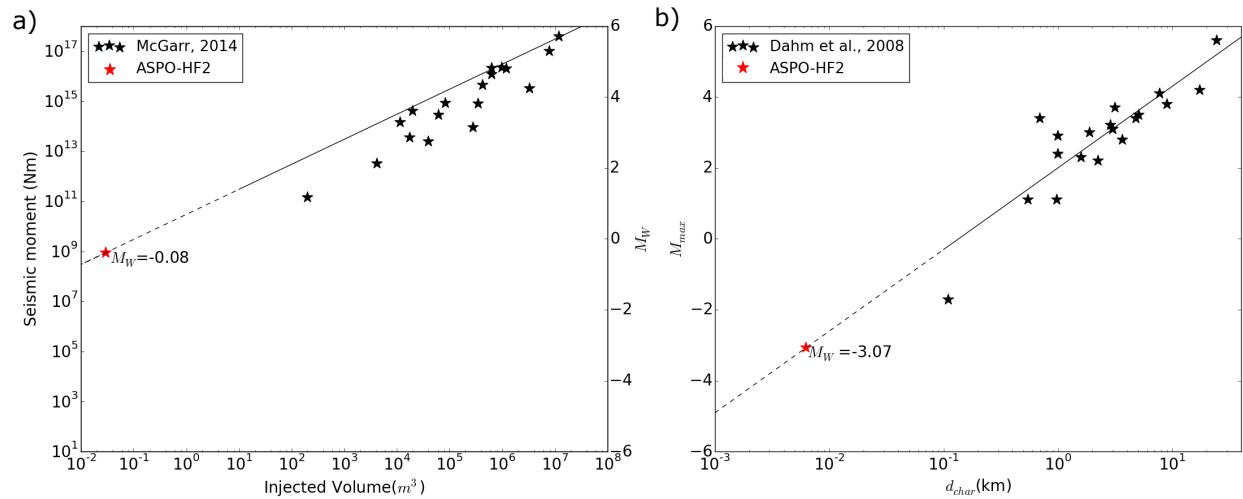


**Figure 14.** a) Maximum seismic moment and magnitude as functions of total volume of injected fluid (in cubic meters) from the start of injection until the time of the largest induced earthquake. Red star shows the point obtained from the HF2 experiment. Black stars correspond with data listed in table 1 from McGarr (2014). Black line solid represent the upper bound seismic moment to the product of the modulus of rigidity and the total volume of injected fluid in figure 2 from McGarr (2014). This line is extended (dashed line) down to very small injected volumes such as in the HF2 experiment. b) The maximal magnitude of fluid-induced earthquake is plotted versus the characteristic length  $d_{char}$  of the fracture (size of the seismicity cloud, estimated as square root of the planar area covered by the cloud). Black stars and black line (empirical relation) correspond with the data for different fracture types from figure 7 in Dahm et al., 2008. Red star shows the point obtained extending the empirical relation (dashed line) to the characteristic length observed in HF2 experiment.

Robust and sufficiently accurate AE locations are reached applying waveform coherence analysis; absolute locations are further improved by relative location using a master event approach (Grigoli et al., 2016). The location quality supports a safe interpretations, in terms of fracture growth and extent. The hydraulic fracturing induced AE activity appears spatially clustered in a prolate ellipsoid, which resembles the main fractured volume ( $\sim 105 m^3$ ). Its principal axes ( $a = 10 m$ ;  $b = 5 m$ ;  $c = 4 m$ ) define the size and orientation (strike  $\sim 123^\circ$ , dip  $\sim 60^\circ$ ). The fracture process exhibits an asymmetric growth with respect to the injection point along the fracturing borehole, which can be interpreted as the result of unequal conditions for fracture growth at opposite sides of the well, e.g. resulting from effective stress gradients of buoyancy effects (e.g. Dahm et al., 2010). AE events generally migrate upwards covering the depth interval between 404 and 414 m. However, at the end of the experiment, the scatter of the AE activity migrates downwards and appears located in the same area of the initial fracture phase, suggesting a crack-closing effect.

## 7. Conclusions

The Äspö mine (Sweden) hydraulic fracturing experiment was first described in its overall layout by Zang et al. (2017), who discussed preliminary findings on induced acoustic emissions, based on triggered recordings. In this work, we analyze the recorded AE signals in much higher detail, focusing on the most seismically productive hydraulic fracturing stage (HF2), and the consequent refracturing. Our study take advantage of a different dataset of continuous recordings, which generation has been specifically planned during the experiment, in order to allow the testing and application of more powerful waveform based methodologies for the detection of AE signals and the location of their sources. We demonstrate the performance of waveform based techniques on continuous very high frequency data. Thanks to the exploitation of the continuous dataset and the implementation of these novel analysis techniques, we successfully improve previous preliminary results and image the fracture process in space and time. The most significant new results of this work are listed below.

- The application of an unsupervised automated full waveform detector applied to the continuous dataset increases the size of the AE catalogue by a factor of  $\sim 40$ , with more than 4000 AEs detected, against 102 AEs for HF2. This size increase of the AE catalogue implies a decrease of the  $M_c$ . However, the improved detection may also concern relatively large AEs, which may be undetected by the triggered-mode operations, if they are preceded by a period of high AE activity.
- A waveform based hypocenter location method (Grigoli et al. 2013, 2014) has been adapted and applied to very high sampled data (1 MHz sampling, against 200 Hz sampling of original applications). Locations have been furthermore refined using a relative, master-event location approach (Grigoli et al., 2016). Furthermore, It is important to note that the KDE provides a novel framework for the quantitative interpretation of massive microseismicity datasets. The large number of AE locations allows to treat the hypocentral cloud in a probabilistic framework, defining the fracture extent on the base of the spatial density of AE sources.
- The large and more complete AE catalogue allowed to perform a more robust analysis of the frequency-magnitude distribution (FMD), which revealed important new results: i) the FMD follows a Gutenberg-Richter law with a high b-value (2.38; 2.57) and  $M_c$  (1.1; 1.61) estimated according to two different techniques (Wiemer and Wyss, 2000; Hainzl, 2016); ii) range of observed magnitudes from 0.77 - 2.79 (magnitude values according to a  $M_{AE}$  scale). We furthermore proof that the high seismicity rates during each frac stage increase temporally  $M_c$  above a basic completeness magnitude: this effect is here observed and quantified for the first time in a hydraulic fracturing process.
- The geometry and extent of the fracture are much better constrained, resembling the main activated fracture volume of about  $105 \text{ m}^3$ . Improved detections and locations allow to see the extension and track the planar rupture also below the injection point down to 414 m depth, instead of 410 m, as previously mapped. Similarly, the increased dataset allows to track the spatiotemporal migration, both among and within fracturing and refracturing stages. For example, we clearly observed a backward migration of hypocenters, after the injection stop, and suggest its relation to the process of closing induced fractures.

- The relation between injected volume and seismicity parameters is discussed: the maximum magnitude in each frac / refrac phase appears to be correlated to the injected volume, whereas we found no correlation between injected volumes and the b-values or the AE rate. A correlation among injected volumes and maximal magnitude support similar empirical observations for injection induced seismicity (McGarr, 2014), but extends it by several magnitude ranges down to the scale of the AE activity
- We discuss observed AE magnitudes and their potential upper bounds in the light of two different approaches to estimate the maximum magnitude during hydraulic fracturing (Figure 14). Whereas the range of observed magnitude satisfy the empirical estimates of maximal magnitude according to both model, the approach of Dahm et al. (2008) appears to be more consistent with our results and more adequate to define the maximal magnitudes when the fluid injection operation produce the opening or reactivation of tensile fractures, rather than the activation of shear failures.

In summary, hydraulic fracturing monitoring with high frequency acoustic emission sensors generates massive dataset recording that could be rapidly analyzed in order to understand the progress and growth of hydraulic fractures. We proofed that waveform stacking and coherence analysis techniques allow detecting and locating automatically AEs, even using very high sampling rates. Our results extend the adoption of similar detection and location techniques, successfully applied for monitoring induced and natural seismic activity at local and regional distances (Matos et al., 2016; López-Comino et al., 2017a) also to very small-scale applications and for hydraulic fracturing, i.e. cm to dm scale fracturing events.

## Acknowledgments and Data

This work is funded by the EU H2020 SHEER project ([www.sheerproject.eu](http://www.sheerproject.eu) - grant agreement No 640896). The in situ experiment (Nova project 54-14-1) was supported by the GFZ German Research Center for Geosciences (75%), the KIT Karlsruhe Institute of Technology (15%) and the Nova Center for University Studies, Research and Development (10%). An additional in-kind contribution of Swedish Nuclear Fuel and Waste Management Co (SKB) for using Äspö Hard Rock Laboratory as test site for geothermal research is greatly acknowledged. Francesco Grigoli is currently funded by the EU H2020 DESTRESS (grant agreement No 691728). The data for this paper are available by contacting A. Zang at [zang@gfz-potsdam.de](mailto:zang@gfz-potsdam.de).

## References

- Baisch S, Harjes, HP (2003) A model for fluid-induced seismicity at the KTB, Germany. *Geophys J Int* 152, 160–170.
- Becker D, Cailleau B, Dahm T, Shapiro S, Kaiser D (2010) Stress triggering and stress memory observed from acoustic emission records in a salt mine. *Geophys J Int* 182, 933–948.
- Beyreuther M, Hammer C, Wassermann J, Ohrnberger M, Megies T (2012) Constructing a hidden Markov model based earthquake detector: Application to induced seismicity, *Geophys. J. Int.*, 189(1), 602–610, doi:10.1111/j.1365-246X.2012.05361.x.
- Bohnhoff M, Dresen G, Ellsworth WL, Ito H (2009) Passive seismic monitoring of natural and induced earthquakes: Case studies, future directions and socio-economic relevance, in *New Frontiers in Integrated Solid Earth Sciences*, pp. 261–285, eds Cloetingh, S.A.P.L. & Negendank, J., Springer.
- Cox SJD, Meredith PG (1993) Microcrack formation and material softening in rock measured by monitoring acoustic emissions. *Int. J. Rock Mech. Min. Sci. Geomech. Abstr.*, 30, 11–24.
- Cesca S, Grigoli F (2015) Chapter Two – Full Waveform Seismological Advances for Microseismic Monitoring. *Advances in Geophysics*, 56, p. 169-228.
- Cesca S, Grigoli F, Heimann S, Dahm T, Kriegerowski M, Sobiesiak M, Tassara C, Olcay M (2016) The Mw 8.1 2014 Iquique, Chile, seismic sequence: a tale of foreshocks and aftershocks. *Geophys J Int*, 204, 3, p. 1766-1780.
- Dahm T (2001) Rupture dimensions and rupture processes of fluid-induced microcracks in salt rock. *J. Volcanol. Geotherm. Res.*, 109(1–3), 149–162.
- Dahm T, Fischer T, Hainzl S (2008) Mechanical intrusion models and their implications for the possibility of magma-driven swarms in NW Bohemia region. *Studia Geophysica et Geodaetica*, 52, 4, p. 529-548.
- Dahm T, Hainzl S, Fischer T (2010) Bidirectional and unidirectional fracture growth during hydrofracturing: Role of driving stress gradients. *J Geophys Res* , 115, B12322.

- Davies R, Foulger GR, Bindley A, Styles P (2013) Induced seismicity and hydraulic fracturing for the recovery of hydrocarbons. *Marine and Petroleum Geology*, 45, 171-185.
- Economides MJ, Nolte KG, Ahmed U, Schlumberger D (2000) *Reservoir Stimulation*, vol. 18, Wiley.
- Eisenblätter J, Spies T (2000) Ein Magnitudenmass für Schallemissionsanalyse und Mikroakustik, *Deutsche Gesellschaft für Zerstörungsfreie Prüfung*, 12, Kolloquium Schallemission, Jena.
- Ellsworth WL (2013) Injection-Induced Earthquakes. *Science*, 341(6142), 1 225 942–1 225 942.
- Fischer T, Hainzl S, Eisner L, Shapiro S, Le Calvez J (2008). Microseismic signatures of hydraulic fracture growth in sediment formations: observations and modeling. *J Geophys Res*, 113, B02307, doi: 10.1029/2007JB005070.
- Fischer, T., S. Hainzl, and T. Dahm (2009), The creation of an asymmetric hydraulic fracture as a result of driving stress gradients, *Geophys. J. Int.*, 179, 634–639, doi:10.1111/j.1365246X.2009.04316.x
- Geiger L (1910) Determination of seismic centres, *Nachrichten von der Koniglicher Gesellschaft der Wissenschaften zu Gottingen Mathematisch Physikalische Klasse, Universitaet Gottingen*, pp. 331–349.
- Goodfellow SD, YoungRP (2014) A laboratory acoustic emission experiment under in situ conditions. *Geophys Res Lett*. 41, doi:10.1002/2014GL059965.
- Grigoli F, Cesca S, Vassallo M, Dahm T (2013) Automated seismic event location by travelttime stacking: An application to mining induced seismicity. *Seismol Res Lett*, 84, 4, 666-677.
- Grigoli F, Cesca S, Amoroso O, Emolo A, Zollo A, Dahm T (2014) Automated seismic event location by waveform coherence analysis. *Geophys J Int* 196, 3, p. 1742-1753.
- Grigoli F, Cesca S, Krieger L, Kriegerowski M, Gammaldi S, Horalek J, Priolo E, Dahm T (2016) Automated microseismic event location using Master-Event Waveform Stacking, *Scientific Reports*, 6, 25744, doi: 10.1038/srep25744
- Gutenberg, R. and C.F. Richter (1944). Frequency of earthquakes in California, *Bulletin of the Seismological Society of America*, 34, 185-188.
- Hainzl, S. (2016): Rate-Dependent Incompleteness of Earthquake Catalogs. - *Seismological Research Letters*, 87, 2A, p. 337-344
- Heimann S, Matos C, Cesca S, Rio I, Custódio S (2017) Lassie: A versatile tool to detect and locate seismicity, in preparation.
- House L (1987) Locating microearthquakes induced by hydraulic fracturing in crystalline rocks. *Geophys Res Lett*, 14(9), 919–921.
- Kochnev V A, Goz I V, Polyakov V S, Murtayev I S, Savin V G, Zommer B K, Bryksin I V (2007). Imaging hydraulic fracture zones from surface passive microseismic data, *First Break*, 25, 77–80.

- Köhler, N., Spies, T., Dahm, T. (2009): Seismicity pattern and variation of the frequency magnitude distribution of microcracks in salt. - *Geophysical Journal International*, 179, 1, pp. 489–499. DOI: <http://doi.org/10.1111/j.1365-246X.2009.04303.x>
- Kwiatek G, Plenkers K, Dresen G (2011) Source Parameters of Picoseismicity Recorded at Mponeng Deep Gold Mine, South Africa: Implications for Scaling Relations. *Bull Seismol Soc Am* 101, 6, 2592-2608.
- López-Comino J A, Cesca S, Kriegerowski M, Heimann S, Dahm T, Mirek J, Lasocki S (2017a) Monitoring performance using synthetic data for induced microseismicity by hydrofracturing at the Wysin site (Poland). *Geophysical Journal International*, 210, 1, p. 42-55.
- López-Comino J A, Heimann S, Cesca S, Milkereit C, Dahm T, Zang A (2017b) Automated Full Waveform Detection and Location Algorithm of Acoustic Emissions from Hydraulic Fracturing Experiment. - *Procedia Engineering*, 191, p. 697-702.
- Madariaga R (1976) Dynamics of an expanding circular fault. *Bull Seismol Soc Am* 66, 639–666.
- Maghsoudi, S., Cesca, S., Hainzl, S., Kaiser, D., Becker, D., Dahm, T. (2013): Improving the estimation of detection probability and magnitude of completeness in strongly heterogeneous media, an application to acoustic emission (AE). - *Geophysical Journal International*, 193, 3, p. 1556-1569.
- Maghsoudi S, Hainzl S, Cesca S, Dahm T, Kaiser D (2014) Identification and characterization of growing large-scale en-echelon fractures in a salt mine. *Geophys J Int* 196, 2, p. 1092-1105.
- Manthei G, Eisenblätter J, Kamlot P (2003) Stress measurements in salt mines using a special hydraulic fracturing borehole tool. *Geotechnical Measurement and Modelling*, pp. 355–360, eds Natau, O., Fecker, E. & Pimentel, E., CRC Press.
- Matos C, Heimann S, Grigoli F, Cesca S, Custódio S (2016) Seismicity of a slow deforming environment: Alentejo, south Portugal, EGU General Assembly 2016, EGU2016-278.
- McGarr A (2014) Maximum magnitude earthquakes induced by fluid injection. *J Geophys Res Solid Earth*, 119, 1008–1019, doi:10.1002/2013JB010597.
- McLaskey GC, Kilgore BD, Lockner DA, Beeler NM (2014) Laboratory generated M -6 Earthquakes. *Pure Appl Geophys* 31, 157-168. doi: 10.1007/s00024-013-0772-9.
- Niitsuma H, Nagano K, Hisamatsu K (1993) Analysis of acoustic emission from hydraulically induced tensile fracture of rock. *J Acoust Emiss*, 11(4), S1–S18.
- Philipp J, Plenkers K, Gärtner G, Teichmann L (2015) On the potential of In-Situ Acoustic Emission (AE) technology for the monitoring of dynamic processes in salt mines. *Mechanical Behaviour of Salt VIII*, pp. 89–98, ed. Roberts, L., CRC Press.
- Rubinstein JL, Mahani AB (2015) Myths and Facts on wastewater injection, hydraulic fracturing, enhanced oil recovery, and induced seismicity. *Seismol Res Lett*, 86(4), 1060–1067.
- Smart KJ, Ofoegbu GI, Morris AP, McGinnis RN, Ferrill DA (2014) Geomechanical modeling of hydraulic fracturing: why mechanical stratigraphy, stress state, and pre-existing structure matter. *Am Assoc Pet Geol Bull* 98(11), 2237–2261.

Suckale J (2009) Induced seismicity in hydrocarbonfields. *Advances in Geophysics*, vol. 51, pp. 55–106, Elsevier, doi:10.1016/S0065-2687(09)05107-3.

Wiemer, S., and M. Wyss (2000), Minimum magnitude of complete reporting in earthquake catalogs: examples from alaska, the western united states, and japan, *Bull. Seismol. Soc. Am.*, 90, 859–869.

Zang A, Oye V, Jousset P, Deichmann N, Gritto R, McGarr A, Majer E, Bruhn D (2014) Analysis of induced seismicity in geothermal reservoirs - An overview. *Geothermics*, 52, 6–21.

Zang A, Stephansson O, Stenberg L, Plenkers K, Milkereit C, Kwiatek G, Dresen G, Schill E, Zimmermann G, Dahm T, Weber M (2017). Hydraulic fracture monitoring in hard rock at 410 m depth with an advanced fluid-injection protocol and extensive sensor array. *Geophys J Int* 208, 2, p. 790-813.